Tomography based numerical simulation of the demagnetizing field in soft magnetic composites

S. Arzbacher,[1] P. Amann,[2] B. Weidenfeller,[3] T. Loerting,[4] A. Ostermann,[5] and J. Petrasch[1,a]

[1]*illwerke vkw Professorship for Energy Efficiency, Vorarlberg University of Applied Sciences, Hochschulstraße 1, 6850 Dornbirn, Austria*
[2]*Department of Physics, Stockholm University, AlbaNova University Center, 10691 Stockholm, Sweden*
[3]*Institute of Electrochemistry, Clausthal University of Technology, Arnold-Sommerfeld-Straße 6, 38678 Clausthal-Zellerfeld, Germany*
[4]*Institute of Physical Chemistry, University of Innsbruck, Innrain 80-82, 6020 Innsbruck, Austria*
[5]*Department of Mathematics, University of Innsbruck, Technikerstraße 13, 6020 Innsbruck, Austria*

The magneto-static behaviour of soft magnetic composites (SMCs) is investigated using tomography based direct numerical simulation. The microgeometry crucially affects the magnetic properties of the composite since a geometry dependent demagnetizing field is established inside the composite, which lowers the magnetic permeability. We determine the magnetic field information inside the SMC using direct numerical simulation of the magnetic field based on high resolution micro-computed tomography data of the SMC's microstructure as well as artificially generated data made of statistically homogeneous systems of identical fully penetrable spheres and prolate spheroids. Quasi-static electromagnetic behaviour and linear material response are assumed. The 3D magnetostatic Maxwell equations are solved using Whitney finite elements. Simulations show that clustering and percolation behaviour determine the demagnetizing factor of SMCs rather than the particle shape. The demagnetizing factor correlates with the slope of a 2-point probability function at its origin, which is related to the specific surface area of the SMC. Comparison with experimental results indicates that the relatively low permeability of SMCs cannot be explained by demagnetizing effects alone and suggests that the permeability of SMC particles has to be orders of magnitude smaller than the bulk permeability of the particle material. © *2015 AIP Publishing LLC*.
[http://dx.doi.org/10.1063/1.4917490]

I. INTRODUCTION

Soft magnetic composites (SMCs) are materials made of ferromagnetic particles mixed with an electrically insulating binder. Although there are some attempts at using molding techniques,[1] the production process usually involves high pressure compaction. This is often followed by curing or by heat treatment if the binder is heat resistant.[2,3] The powder-like nature of SMCs results in isotropic ferromagnetic behaviour, which promises more freedom in the design of electrical devices compared to the anisotropic character of laminated steel. Additionally, the insulating substrate material prevents the formation of macroscopic current paths and thus eddy current losses are small even at high frequencies.[4,5] Despite a generally low permeability and high total core losses at low frequencies, SMCs are attractive materials for a broad range of applications in a wide frequency spectrum because of cost benefits in the production process. These applications include electric motors, actuators, and sensors as well as induction heaters, inductors, and even microwave devices.[6–10] A thorough understanding of SMCs' electric and magnetic properties is crucial for manufacturers as well as engineers. The effect of mixing ratios and constituent particle properties on the magnetic response of the composite is one of the open

questions and has been recently discussed by Anhalt and Weidenfeller[11–13] and others.[14–16] Another question of interest is the effect of strain and tension, usually involved in the production process, on the electromagnetic properties and was addressed by Hemmati *et al.*[17] and Taghvaei *et al.*[18] for dense SMCs and Brosseau *et al.*[19,20] for filled polymers.

Several models for heterogeneous magnetic materials that relate particle permeability, particle shape, and filler fraction to effective magnetic properties have been developed.[21–27] Due to the mathematical analogy of electric permittivity and magnetic permeability in static systems,[28] these models are closely related to the well known models for electrically heterogeneous materials. These results[29–32] also lead to a better understanding of magnetic phenomena and vice versa. Ferromagnetic particles repel magnetic fields and form shape dependent demagnetizing fields, reducing the particle's permeability. Thus, in most models, the influence of particle shape on magnetic properties is accounted for by demagnetizing factors. This is the magnetic analogy to a depolarizing field reducing the electric field inside a particle, which is also often described by the depolarization factor. For regular geometrical objects, such as ellipsoids, prisms, or rods, these factors are well known from theoretical or numerical analysis.[33–37] In most models of composites, ellipsoids are used to represent any particle shape since they form homogeneous demagnetizing fields. This results in analytical expressions mapping particle permeability, demagnetizing

a)Author to whom correspondence should be addressed. Electronic mail: joerg.petrasch@fhv.at. Tel.: +43 5572 792 3801.

factor, and filler fraction to the corresponding quantities of the composite.

Although most models do not directly consider magnetic field perturbation in the neighbourhood of particles caused by their demagnetizing field, a significant fraction of particles is influenced by their neighbours' demagnetizing fields (even in low density SMCs).[38–41] Hence, the microstructure complicates modelling and greatly affects properties like magnetic susceptibility and ferromagnetic resonance frequency.

The objective of the current work is to determine the influence of the irregular microstructure of an SMC on the demagnetizing field represented by the demagnetizing factor. We use X-ray micro-computed tomography (μCT)[42] to determine the material's three-dimensional structure. A *GE nanotom-m*[43] high resolution μCT system capable of voxel sizes of 1 μm^3 and less is used. Subsequently, a 3D unstructured tetrahedral grid is generated using the measured geometry and a tetrahedral mesh generator based on space indicator functions developed by Friess *et al.*[44] Extensive numerical simulations of the magnetostatic behavior are carried out using Whitney elements[45] as implemented in the open source finite element method (FEM) software ELMER.[46] The numerical simulation provides detailed 3D electromagnetic field information within and outside the SMC, which is solely based on geometry data and magnetic permeabilities of individual phases. Hence, the demagnetizing factor can be investigated independent of non-geometric phenomena, and experimental uncertainties. The combination of μCT and numerical simulation is referred to as tomography based numerical simulation (TBNS). It has been applied to radiative transfer,[47] conductive heat transfer,[48] and fluid flow[49] in a range of different materials. To the best of our knowledge, this is the first time that TBNS is applied to magnetic phenomena. We used two sample sets, which were experimentally investigated by Anhalt *et al.*[50] For reference, a few numerical studies on randomly generated data are done and compared with the results of the sample sets and the already published numerical work of Mattei and Le Floc'h.[25]

II. THEORY

A. Vector component volume average

Consider an SMC occupying the region $\mathcal{V}$ which can be decomposed into the two disjoint regions $\mathcal{V}_\mathrm{m}$ and $\mathcal{V}_\mathrm{d}$ such that $\mathcal{V} = \mathcal{V}_\mathrm{m} \cup \mathcal{V}_\mathrm{d}$ and $\mathcal{V}_\mathrm{m} \cap \mathcal{V}_\mathrm{d} = \emptyset$. The subscripts m and d refer to the magnetic and dielectric (nonmagnetic) material phase, respectively. The volume average of the kth vector component of the vector field $\mathbf{v} : \mathcal{V} \mapsto \mathbb{R}^3$ on the region $\mathcal{V}_\mathrm{m}$ is defined by

$$(\overline{v_k})_\mathrm{m} := \frac{\int_{\mathcal{V}_\mathrm{m}} v_k \mathrm{dV}}{|\mathcal{V}_\mathrm{m}|}. \tag{1}$$

According to the used standard basis $\{\mathbf{e}_x, \mathbf{e}_y, \mathbf{e}_z\}$ subscript k can either be x, y, or z and will be reserved for that purpose further on. $|\mathcal{V}_\mathrm{m}|$ denotes the volume of the region $\mathcal{V}_\mathrm{m}$. This definition will help to describe the demagnetizing factor in a concise fashion.

B. Demagnetizing factor

In a complete magnetic circuit and under the assumption of linear material response, the magnetic flux density $\mathbf{B}$ is related to an exciting magnetic field $\mathbf{H}_0$ via the relative permeability μ_r

$$\mathbf{B} = \mu_0(\mathbf{H}_0 + \mathbf{M}) = \mu_0 \mu_\mathrm{r} \mathbf{H}_0. \tag{2}$$

Thus, for linearly responding material the magnetization $\mathbf{M}$ of the ferromagnetic material is related to the magnetic field strength $\mathbf{H}$, which is magnetizing the material, by the linear law

$$\mathbf{M} = \chi\mathbf{H} = (\mu_\mathrm{r} - 1) \times \mathbf{H}, \tag{3}$$

where χ denotes the magnetic susceptibility. In noncomplete magnetic circuits, the demagnetizing field $\mathbf{H}_D$ reduces the magnetic field inside the ferromagnetic material and Eq. (2) becomes

$$\mathbf{B} = \mu_0(\mathbf{H}_0 + \mathbf{M} + \mathbf{H}_D). \tag{4}$$

Due to the microgeometry of SMCs non-complete circuits have to be considered, even for toroidal cores.

Let us now consider an SMC of regular shape, e.g., an ellipsoid or a cylinder, completely immersed in a uniform magnetic field $\mathbf{H}_0$ applied along one of the principle directions $\mathbf{e}_k$. The orientation in space of the SMC is assumed to be well defined and fixed. Using the notation introduced in Subsection II A, the *total magnetometric demagnetizing factor* N_k^tot along direction $\mathbf{e}_k$ is defined[34] by

$$(\overline{H_{D,k}})_\mathrm{m} = -N_k^\mathrm{tot} \times (\overline{M_k})_\mathrm{m}. \tag{5}$$

Note that in the case of bulk ellipsoids N_k^tot is consistent with the well known demagnetizing factors for ellipsoids but it also covers non-uniform demagnetizing fields, e.g., in cylinders. The term *magnetometric* is deduced from magnetometer measurements and will be dropped hereafter. By taking the vector component volume average Eq. (4) transforms to

$$(\overline{B_k})_\mathrm{m} = \mu_0[(\overline{H_{0,k}})_\mathrm{m} + (1 - N_k^\mathrm{tot}) \times (\overline{M_k})_\mathrm{m}]. \tag{6}$$

In analogy to Eq. (2), an intrinsic permeability $\mu_{k,\mathrm{m}}$ of the magnetic phase of the SMC is defined by

$$(\overline{B_k})_\mathrm{m} = \mu_0 \mu_{k,\mathrm{m}} (\overline{H_{0,k}})_\mathrm{m}. \tag{7}$$

This can be understood as the magnetic permeability corrected by the intrinsic demagnetization. Since in noncomplete circuits the magnetic field acting on the material is $\mathbf{H} = \mathbf{H}_0 + \mathbf{H}_D$ volume averaging and Eq. (3) leads to the self consistent law

$$(\overline{M_k})_\mathrm{m} = (\mu_\mathrm{r} - 1) \times [(\overline{H_{0,k}})_\mathrm{m} - N_k^\mathrm{tot} \times (\overline{M_k})_\mathrm{m}]. \tag{8}$$

Combining Eqs. (6), (7), and (8) the total demagnetizing factor N_k^tot (abbreviated with total DMF) of the magnetic material phase becomes

$$N_k^{\text{tot}} = \frac{(\mu_{\text{r}}/\mu_{k,\text{m}}) - 1}{\mu_{\text{r}} - 1}, \qquad (9)$$

where μ_{r} is the relative permeability of the magnetic bulk also measured in complete magnetic circuits.[51] The only total DMF of interest in the course of this work will be N_z^{tot}. Therefore, the notation will be simplified by the definition $N^{\text{tot}} := N_z^{\text{tot}}$. As mentioned above, not only ring shaped SMCs but also samples with finite sizes and regular outer shapes are considered. In order to distinguish the demagnetizing effects caused by the composites' outer shape from the demagnetizing effects caused by the inner structure, it is useful to decompose the total DMF into the inner DMF N^{inn} and the geometric DMF N^{geo} such that

$$N^{\text{tot}} = N^{\text{inn}} + N^{\text{geo}}. \qquad (10)$$

The geometric DMF depends on the external shape of the SMC alone, while the inner DMF incorporates the SMCs microstructure. Hence, in bulk material N^{inn} vanishes almost completely[50,52] and N^{tot} is governed by the external shape of the specimen. On the other hand, N^{geo} vanishes in toroids, infinitely long cylinders or prisms when their axis is aligned along the exciting field direction.[21] In all other cases, a geometric demagnetization factor due to free magnetic poles at the surface of the composite, and additionally an inner demagnetization factor due to free poles on particles and/or agglomerates within the composites appears.[21,25,40] As a result, the permeability of the material is reduced to an apparent permeability by the demagnetizing fields. Following Eq. (7) an apparent permeability $\mu_{k,\text{app}}$ of the inscribed SMC sample including the non-magnetic material phase can be defined by averaging over the SMC's entire volume instead. The apparent permeability $\mu_{k,\text{app}}$ is also the one measured in experiments. The only apparent permeability of interest will be $\mu_{z,\text{app}}$ and thus the simplification $\mu_{\text{app}} := \mu_{z,\text{app}}$ is made.

C. Directional 2-point probability function

A first approach to the analysis of the microstructure of SMCs is motivated by the theory of random heterogeneous materials (RHMs).[28] For sufficiently large samples, i.e., considerably larger than the correlation length of the quantity in question, the methods of the RHM theory can be applied to investigate single SMCs.[28]

Using the denomination given in Subsection II A, the indicator function $\mathcal{I}(\mathbf{x})$ for the magnetic material phase is

$$\mathcal{I}(\mathbf{x}) = \begin{cases} 1 & \text{for } \mathbf{x} \in \mathcal{V}_{\text{m}} \text{ and} \\ 0 & \text{in any other case.} \end{cases} \qquad (11)$$

The probability of finding two points $\mathbf{x}_1$ and $\mathbf{x}_2 \in \mathcal{V}$ separated by $\mathbf{x}_1 - \mathbf{x}_2 = r\,\mathbf{v}$ in $\mathcal{V}_{\text{m}}$ is the *directional 2-point probability function*

$$\hat{S}_2(r\,\mathbf{v}) := \frac{\int_{\mathcal{V}} \mathcal{I}(\mathbf{x}) \times \mathcal{I}(\mathbf{x} + r\,\mathbf{v})\,d\mathbf{x}}{|\mathcal{V}|}, \qquad (12)$$

where r is a radial distance along the direction given by the unit vector $\mathbf{v}$. Hence, the probability of finding two points $\mathbf{x}_1$ and $\mathbf{x}_2 \in \mathcal{V}$ with distance $||\mathbf{x}_1 - \mathbf{x}_2|| = r$ in $\mathcal{V}_{\text{m}}$ is

$$S_2(r) := \frac{\int_{\partial B} \hat{S}_2(r\,\mathbf{v})\,d\mathbf{v}}{4\pi r^2}, \qquad (13)$$

which is called the *2-point probability function*. The set $\partial B = \{\mathbf{v} \in \mathbb{R}^3 : ||\mathbf{v}|| = 1\}$ denotes the boundary of the unit ball, and $4\pi r^2$ is the surface area of the sphere with radius r. Note that usually periodic boundary conditions are applied when $\mathbf{x} + r\,\mathbf{v}$ leaves the region $\mathcal{V}$ of the soft magnetic composite sample.

In the case of isotropic random materials, the *specific surface area* of a two-phase material can be derived from the slope of $S_2(r)$ at its origin.[28] Analogously we define a *directional specific surface area*

$$\hat{s}_{\mathbf{v}} := \frac{d}{dr} \hat{S}_2(r\,\mathbf{v})\big|_{r=0}. \qquad (14)$$

This can be interpreted as a projection of the specific surface area on a plane orthogonal to direction $\mathbf{v}$ (cf. Fig. 1). Note that $\hat{S}_2(r\,\mathbf{v})$ as well as $S_2(r)$ do not provide information about percolating clusters.[28]

Given a 3D voxel dataset representing the discretized space of a heterogeneous material, $\hat{S}_2(r\,\mathbf{v})$ is obtained by Monte Carlo integration.[28]

III. MATERIALS AND METHOD

A. Sample material

An irregularly shaped iron powder (Fe, ASC100.29, Höganäs AB, Sweden, $\mu_{\text{r}} = 10^3$) mixed with polypropylene and a needle shaped nano-crystalline powder (Finemet, Arcelor S.A., Luxembourg, $\mu_{\text{r}} = 10^5$) mixed with wax are investigated for several filler fractions. Identical materials were used in an experimental study by Anhalt *et al.*[50] Note that the Finemet samples with filler fraction $x = 0.2$ and $x = 0.6$ were not available and could not be investigated in this study. The sample dimensions are approximately $3 \times 3 \times 15\,\text{mm}^3$.

B. Microtomography

μCT images of the samples are obtained using the *GE nanotom-m*[43] high resolution tomography setup at the
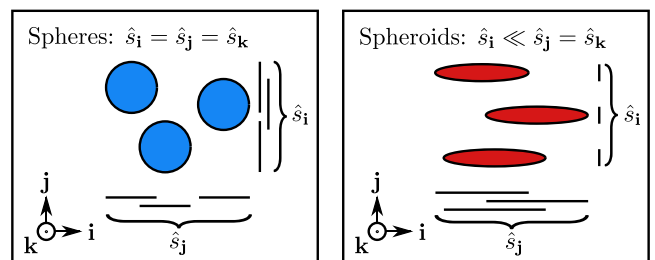
FIG. 1. Sketches of the directional specific surface area $\hat{s}_{\mathbf{v}}$ for sphere and spheroid packings for constant filler fraction x along directions $\mathbf{i}$, $\mathbf{j}$, and $\mathbf{k}$.
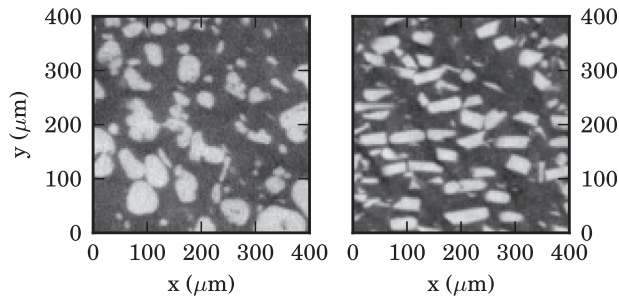
FIG. 2. Tomography slices of Fe (left) and Finemet (right) samples both for a filler fraction of $x = 0.3$. Particles are bright, matrix is dark.

Vorarlberg University of Applied Sciences. Image stacks representing slices of the three-dimensional structure—as shown in Fig. 2—are reconstructed in the μCT process.

In Tables I and II, the scan parameters employed are shown. All scans are done with full sample rotation along a fixed axis.

C. Segmentation

The CT scans generally are of good quality with low noise and a high contrast between the grey scale values of the two material phases (cf. Fig. 2). Beam hardening effects were corrected by a proprietary GE algorithm. Particle diameters are significantly larger than the voxel sizes used. Since the reconstructed images are homogeneous throughout, as is the whole image stack, a local segmentation approach[53,54] is unnecessary. Therefore, a simple binary threshold filter is used to segment the reconstructed images into magnetic and dielectric phases. The global threshold value is chosen by equalizing the filler fraction x of the digital data with the known filler fraction of the original sample. Representative spherical and cylindrical subsets of the data are selected for further processing which is necessary because of computational limitations. This selection involves two steps: (1) a manual preselection is done such that there are no inhomogeneities in particle distribution visible to the human eye. (2) 2-point probability functions are computed to obtain the correlation length

TABLE I. CT parameters for Fe samples for filler fractions x.

x	0.1	0.2	0.3	0.4
Tube voltage (kV)	150	150	160	160
Magnification (-)	25	70	58	44
No. of images (-)	1000	1700	1700	1700
Exposure time per image (ms)	2000	1250	2000	2000
No. averaged images (-)	4	4	3	3
Voxel edge length (μm)	3.99	1.41	1.71	2.26
x	0.5	0.6	0.7	0.8
Tube voltage (kV)	160	160	160	160
Magnification (-)	50	54	50	50
No. of images (-)	1700	1700	1700	1700
Exposure time per image (ms)	2000	1500	1500	1500
No. averaged images (-)	3	4	4	4
Voxel edge length (μm)	2.0	1.86	2.0	2.0

TABLE II. CT parameters for Finemet samples for filler fractions x.

x	0.1	0.3	0.4	0.5
Tube voltage (kV)	120	90	90	90
Magnification (-)	57	53	84	84
No. of images (-)	2000	1900	1800	1800
Exposure time per image (ms)	1500	2000	2000	2000
No. averaged images (-)	4	4	4	4
Voxel edge length (μm)	1.75	1.87	1.19	1.99

$$l_{\text{corr}} = \min\{r > 0 \,|\, \forall r' \geq r : |S_2(r') - x^2| \leq x/50\} \quad (15)$$

of the magnetic particles. A cubic volume $V \geq (3\,l_{\text{corr}})^3$ is then accepted as representative. Note that due to statistical fluctuations in the particle distribution, the filler fractions of the subsets can slightly differ from those of the full dataset.

D. Mesh generation

The data subsets together with a cylindrical shell are then inscribed into a cuboid. Mesh generation is subsequently carried out.[44] Three different types A, B, and C of meshes are created to investigate spherical, cylindrical, and infinitely long SMC shapes (cf. Figs. 3 and 4). The dimensions of the volumes investigated are determined such that the SMC subset used for simulation is statistically relevant while the numerical error remains small, i.e., the tetrahedra are sufficiently small. The combination of these requirements results in a mesh with regions of severely different mesh density, e.g., tetrahedra inside the SMC subset are refined seven times, whereas tetrahedra at the boundary ∂A_{xy} are untouched. To account for the difference in mean particle diameter of Fe and Finemet samples, the mesh types are scaled to two sizes I and II. The required mix of mesh types and sizes produces overall four configurations whose dimensions are given in Table III. This computational setup is necessary to simulate SMCs of finite size and a regular outer shape, which is impossible with a unit-cell based periodic structure.

E. Computer generated SMCs

As reference, artificial SMCs are computer generated. They are created by packing identical fully penetrable spheres[28] or prolate spheroids (ellipsoids with semi axes
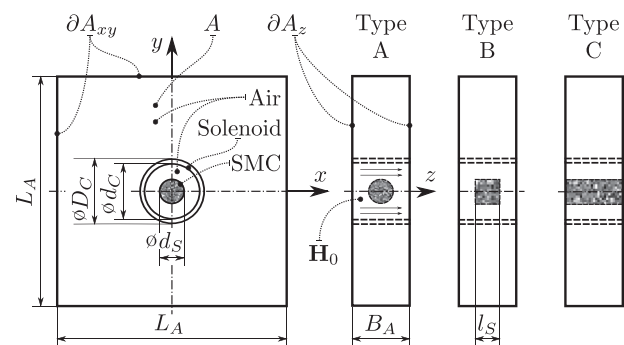

FIG. 3. Scheme of the simulation configurations. The grey regions represent the SMC whereas the white cuboid models a surrounding of air in which a homogeneous field is created by a continuous solenoid.
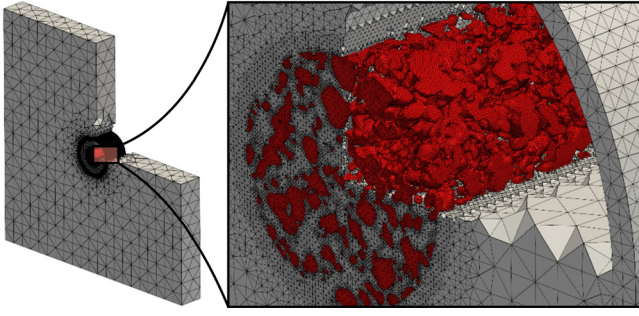
FIG. 4. Example mesh of a type CI simulation configuration based on the microgeometry of an Fe SMC with $x = 0.4$.

$c > b = a$) into prescribed SMC shapes using random center points. This packing is also known as the "Swiss-cheese" model and creates spatially uncorrelated spheres/spheroids, which may overlap.[55] In case of the spheroids, two configurations are considered: (1) the major axis of each single spheroid is oriented along the exciting field axis (z-axis) and (2) the major axis of single spheroids is randomly oriented along either x, y, or z-axis. Filler Fractions x, in the range $[0.01, 0.95]$, are investigated. Equation (16) gives a useful estimate for the total number n_S of identical overlapping spheres or spheroids of volume V_S for a given filler fraction x packed in a region with volume V_{SMC} (Refs. 28 and 56):

$$n_S(x) = -\ln(1 - x) \times \frac{V_{\text{SMC}}}{V_S}. \tag{16}$$

Preliminary simulations showed that the DMFs of randomly packed SMCs with an identical number of spheres or spheroids and filler fractions $x \leq 0.35$ significantly deviated. Contrary, above that filler fraction the deviation from the mean value remains below 5%. To account for this deviation, each data point for filler fractions $x \leq 0.35$ is computed as the mean of six different mesh realizations with the same number of packed particles. For $x > 0.35$, the data points originate from one single realization. The deviation limiting value $x = 0.35$ is in remarkable good agreement with the theoretical value $x_P = 1/3$ for the percolation threshold predicted by a Bruggemann-Landauer's type effective medium theory (EMT).[57] Recent results by Torquato and co-workers reported a percolation threshold in three dimensional space of $x_P = 0.3418$.[58,59] This threshold is the same for overlapping spheres and oriented spheroids.[60] The observed maximum deviation for $x \leq 0.35$ is $\Delta \hat{N}^{\text{tot}} = 0.033$. It shall be noted that the deviation is largest for small filler fractions

TABLE III. Mesh dimensions of the four mesh configurations.

	l_s (μm)	d_S (μm)	B_A (μm)	L_A (μm)	D_C (μm)	d_C (μm)
Type AI	...	1000	5000	13333	2167	2000
Type BI	1400	350	5000	13333	2167	2000
Type CI	...	350	1400	13333	2167	2000
Type CII	...	350	700	6667	1083	1000

and decreases with an increase of the filler fraction. A possible explanation for this is the relatively small number of particles used for small filler fractions. The number of particles for larger filler fractions is significantly higher which leads to better statistics. Additionally, the influence of the microstructure on the DMF may be suppressed by the effects of clustering which increases with increasing filler fraction. Packed spheroids with oriented major axis result in less deviation than spheres or spheroids with unoriented major axis.

F. Simulation model

A homogeneous magnetic field, created by the current density $\mathbf{j}_s = j_0 \left(-y, x, 0 \right)^T$ inside the solenoid, is applied in axial direction of the air cylinder containing the SMC subset. The magnetic flux density $\mathbf{B}$ is determined by solving the 3D magnetostatic Maxwell equations for a linear constitutive law

$$\begin{aligned} \text{curl } \mathbf{H} &= \mathbf{j}, \\ \mathbf{B} &= \mu_0 \mu \, \mathbf{H}, \\ \text{div } \mathbf{B} &= 0, \end{aligned} \tag{17}$$

inside the computational domain A (cf. Fig. 3). The boundary conditions are

$$\begin{aligned} \mathbf{n} \times \mathbf{H} &= 0 \quad \text{on} \quad \partial A_{xy}, \\ \mathbf{n} \cdot \mathbf{B} &= 0 \quad \text{on} \quad \partial A_z, \end{aligned} \tag{18}$$

where $\mathbf{n}$ denotes the outer-pointing normal vector. The relative permeability μ is a function of position which equals one in the case of air or nonmagnetic binder or which is $\mu_r > 1$ in case of magnetic material. The open source multiphysics FEM software ELMER[46] is used to compute the flux density $\mathbf{B}$ using *Whitney* elements and a vector potential formulation of Eq. (17). Once the magnetic flux density is known the DMF is computed as described in Sec. II B.

G. Simulation

Simulations with single spheres are carried out to estimate the relative error of the numerical method used. DMFs $\hat{N}^{\text{geo}}$ (equal to $\hat{N}^{\text{tot}}$ in this setting) of bulk spheres with diameters $d_S \in \{33, 67, 100, 133, 267\} \mu$m are computed in type AI simulations on meshes with minimal edge lengths of $d_{\text{min}} \in \{4.2, 5.0, 6.7, 8.3, 10.0, 13.3, 16.7\} \mu$m and then compared to the exact factor $N = 1/3$. Note that the circumflex in $\hat{N}$ will be used hereafter to point out that the value stems from the simulation results. In Fig. 5, the relative error $|(\hat{N}^{\text{geo}} - N)/N|$ is shown with respect to the inverse of the minimal edge length d_{min}. The reference lines of slope -2 suggest quadratic convergence of the FEM. This means the relative error is bounded by $C d_{\text{min}}^2$ for d_{min} sufficiently small and some constant C independent of d_{min}. Simulations based on cylinders with a length to diameter ratio of $2:1$ also show quadratic convergence and comparable relative errors. Meshes with a minimal edge length of 5 μm in size I configurations and 2.5 μm in size II configurations, indicated by a dashed vertical line in Fig. 5, are used throughout the rest of this paper. These lead to relative errors of approximately 5%
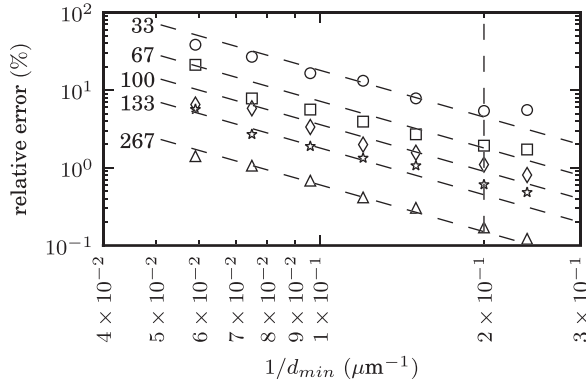
FIG. 5. Relative errors of simulated geometric DMFs of single full spheres with diameters $d_S \in \{33, 67, 100, 133, 267\}\mu m$. They are obtained from type AI simulations on meshes with varying minimal edge lengths $d_{\min} \in \{4.2, 5.0, 6.7, 8.3, 10.0, 13.3, 16.7\}\mu m$. Reference lines of slope -2 are added to illustrate the quadratic convergence rate of the FEM.

for small objects and to significantly lower relative errors for all larger objects. Small objects can have dimensions down to only seven times the shortest edge.

The typical mesh size is about 10^7 elements, which requires approximately 128 GB of memory: the Whitney elements method is known for its high memory consumption. Mesh generation takes about three hours per mesh, while the total solver run-time on 32 cores does not exceed one hour. Simulation results are visualized with SALOME.[61] Post processing is done using vtk-libraries.[62]

H. Overall processes

For reasons of clarification we distinguish between the AGBNS (artificial geometry based numerical simulation) and the TBNS (tomography based numerical simulation) process. The AGBNS process solely uses computer generated geometries and follows the workflow *generation of sphere/spheroid packings–mesh generation–numerical simulation*. Real SMCs are studied using the TBNS process described by the workflow *μCT scan–segmentation–mesh generation–numerical simulation*. Figure 6 shows the result of the TBNS process–detailed magnetic field information inside an SMC whose geometry was captured by μCT.
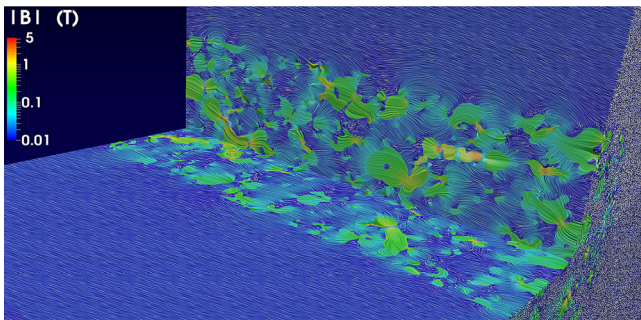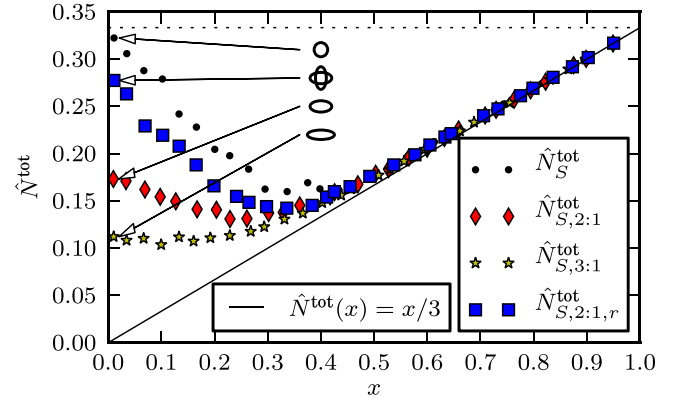

FIG. 6. Cross sectional visualization of the magnetic flux density in an SMC. The field is the result of a simulation of a type CI configuration based on μCT scans of an Fe sample with a filler fraction of $x = 0.3$.
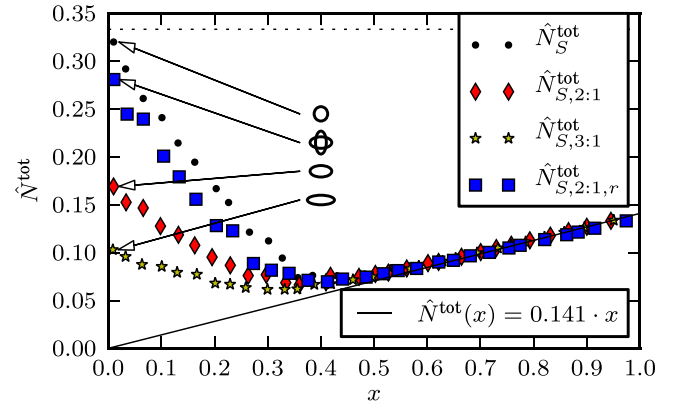
IV. RESULTS

A. Randomly packed spheres and spheroids

In Figs. 7(a)–7(c), the DMFs of artificial SMCs resulting from a comprehensive series of AGBNS processes are shown.
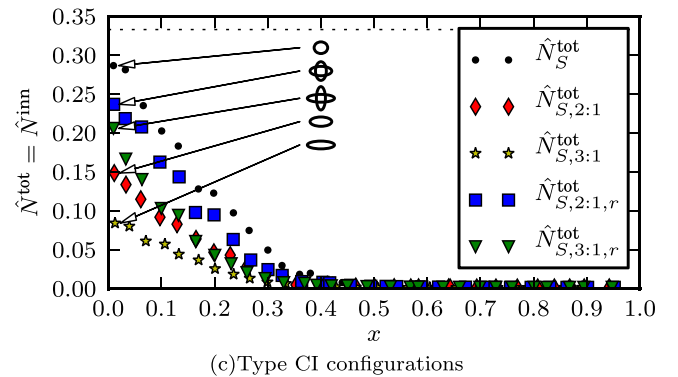
Figure 7(a) shows the results of type AI simulation series. $\hat{N}_S^{\text{tot}}$ is the DMF of randomly packed spherical

(a) Type AI configurations

(b) Type BI configurations

(c) Type CI configurations

FIG. 7. DMFs of randomly packed spheres ($\hat{N}_S^{\text{tot}}$) and oriented and unoriented prolate spheroids ($\hat{N}_{S,2:1}^{\text{tot}}, \hat{N}_{S,3:1}^{\text{tot}}, \hat{N}_{S,2:1,r}^{\text{tot}}$, and $\hat{N}_{S,3:1,r}^{\text{tot}}$) obtained from simulations of types AI, BI, and CI configurations for various filler fractions x. The subscripts $2:1$ and $3:1$ refer to the ratio of major to minor axis, while subscript r in $\hat{N}_{S,2:1,r}^{\text{tot}}$ and $\hat{N}_{S,3:1,r}^{\text{tot}}$ indicates the random direction of the major axis which is either oriented along the x, y, or z-axis. In the case of oriented spheroids, the major axis is aligned in direction of the solenoid axis. The major axis length for aspect ratio $2:1$ is $l_P = 80\,\mu m$ and $l_P = 100\,\mu m$ for an aspect ratio of $3:1$. Spheres' diameters are $d_P = 50\,\mu m$. The assumed relative permeability of the magnetic material is $\mu_r = 1000$.

particles with particle diameter $d_P = 50\,\mu m$. The points $\hat{N}^{\text{tot}}_{S,2:1}$, $\hat{N}^{\text{tot}}_{S,2:1,r}$, and $\hat{N}^{\text{tot}}_{S,3:1}$ are the DMFs of packed prolate spheroids. If the filler fractions are low and approaching a value $x \to 0$, the theoretically calculated values for spheres ($N_S = 1/3$) can be observed for the simulations of single spheres (cf. bullets in Fig. 7(a)). This observation is also made analogously for oriented single spheroids with aspect ratios of 2 : 1 (cf. diamonds in Fig. 7(a)) and 3 : 1 (cf. stars in Fig. 7(a)) which reproduce theoretical values of $N_{S,2:1} = 0.1736$ and $N_{S,3:1} = 0.1087$, respectively.[21,35] Randomly packed spheroids tend to a DMF of $\hat{N}^{\text{tot}}_{S,2:1,r} = 0.28$ for a filler fraction approaching $x \to 0$. This value corresponds to a spheroid with an aspect ratio of 5 : 4.[21] However, this difference in the values of spheres and unoriented spheroids for $x \to 0$ can be ascribed to the low number of particles. A higher number of randomly packed spheroids would finally lead to a quasi-spherical particle with a DMF of $N_S = 1/3$. This would simultaneously require a much larger volume to retain the low filler fraction. Hence, it can be assumed, that the calculated values also represent "real" SMCs with randomly oriented spheroids at low filler fractions, because an agglomeration of the spheroids to one big "quasi-spheroid" is unlikely. With increasing filler fraction the DMFs of the investigated particle configurations equalize more and more. For $x = 0.4$, the calculated DMFs are nearly independent on the particle's shape and orientation. The DMFs of the SMC asymptotically approach the straight line $\hat{N}^{\text{tot}}(x) = x/3$ and almost coincide with that line for $x \geq 0.5$. Extrapolation to $x = 1$ yields the DMF $\hat{N}^{\text{tot}}(1) = 1/3$ of the fully packed SMC, which is the DMF of a sphere–the shape of the SMC in the simulated configuration.

The results of a type BI simulation series are shown in Fig. 7(b). The only difference to the configuration in Fig. 7(a) is the SMC's shape which has changed from a sphere to a cylinder with length to diameter ratio $l_S/d_S = 2$ (cf. Fig. 3). The configurations of the packed fully penetrable spheres and spheroids are as described above. The DMFs of the sphere and spheroid packings exhibit the same behaviour as in Fig. 7(a). However, the DMFs asymptotically approach the straight line $\hat{N}^{\text{tot}}(x) = 0.141 \times x$. They are very close to this line for $x \geq 0.5$. Thus, for the fully packed SMC one finds $\hat{N}^{\text{tot}}(1) = 0.141$, which is the DMF of a cylinder with $l/d = 2$ and magnetic susceptibility $\chi = 1000$.[21,34] This is consistent with the configuration simulated.

Figure 7(c) shows the results of a type CI simulation series modeling infinitely long cylindrical SMCs. In an infinitely long cylinder, the DMF for bulk material vanishes. This implies that in all type C configurations the DMF is solely determined by the microstructure. Therefore, in type C configurations $\hat{N}^{\text{tot}} = \hat{N}^{\text{inn}}$ and the term inner DMF can be used equivalently. An additional simulation series is done to compute the inner DMFs of artificial SMCs filled with unoriented overlapping spheroids whose center points and orientations are uniformly distributed as already described above. They have an aspect ratio of 3 : 1 and a major axis length of $l_P = 100\,\mu m$ and are denoted by $\hat{N}^{\text{tot}}_{S,3:1,r}$ (triangles in Fig. 7(c)). In all SMC packings used, the DMFs are almost zero for $x > 0.4$. This is again in good agreement with the configuration simulated. For filler fractions $x < 0.4$, the DMFs are

slightly smaller than those resulting from type AI and type BI simulations. The values extrapolated to $x \to 0$ underestimate the expected results by approximately 0.02. This can be explained by the fact that all particles in type CI simulations, which are cut by the SMC boundary, become thinner, which corresponds to a higher ratio of major to minor axis. The unoriented spheroid packings (subscript r) with aspect ratio 2 : 1 (cf. squares in Fig. 7(c)) show a larger DMF than those with aspect ratio 3 : 1 (cf. triangles in Fig. 7(c)) for $x < 0.4$. Also the slope of the DMFs of unoriented spheroid packings with aspect ratio 2 : 1 at the origin is slightly larger than those of spheroid packings with aspect ratio 3 : 1. The differences of the DMFs of unoriented spheroids and spheres for $x \to 0$ are already discussed above. However, the difference of slope of the calculated values for $x \leq 0.4$ is assumed to be the result of different affinities to clustering.

Recalling the decomposition of the DMF described in Eq. (10) two essential observations become apparent in this subsection: (1) In the limit $x \to 0$ particles do not interact. The macroscopic shape of the SMC has no influence on the DMF which is completely governed by the shape of the particles used. In this limit, $\hat{N}^{\text{geo}} = 0$ and $\hat{N}^{\text{inn}}$ is the statistical mean of the geometric DMFs of the particles used. (2) Regardless of the used particle shape the DMFs asymptotically approach a straight line $\hat{N}^{\text{tot}}(x) = N^{\text{geo}} \times x$ where N^{geo} is the geometric DMF of the SMCs external shape. For a particle permeability of $\mu_r = 1000$, the DMFs are very close to that line for $x \geq 0.4$. Mattei and Le Floc'h[25] explain the decrease of the DMF (cf. Fig. 7(c)) with the formation of clusters of increasing size until the cluster size diverges at the percolation threshold. In contrast to their results no percolation "jump" can be found in Fig. 7. In the current work, the DMF is defined with respect to the magnetic material phase only, while Mattei and Le Floc'h define the DMF with respect to the whole sample. Since the DMF is completely governed by the external shape of the SMC once $x \geq 0.4$ we consider $x = 0.4$ as the percolation threshold. This is in good agreement with the results of Mattei and Le Floc'h[25] and slightly larger than the geometrical percolation threshold $x_P = 0.3418$. The surprisingly simple linear lower bound, $\hat{N}^{\text{tot}}(x) = N^{\text{geo}} \times x$, cannot be rigorously explained at this time.

Figure 8 compares the inner DMFs of two simulation series, which are done in a type CI configuration for two different values of the particle permeability μ_r. It can be seen that the DMF decreases faster for a given particle shape when the particle permeability is higher, which is in accordance to the results of Mattei and Le Floc'h.[25] Especially, it can be observed that the DMFs vanish for filler fractions larger than approximately 0.4 when a particle permeability of $\mu_r = 1000$ is assumed, while for a particle permeability of $\mu_r = 20$ DMFs remain larger than zero until a filler fraction of $x \approx 1$ is reached.

The results shown are based on the numerical solution of Maxwell's equations and can be understood qualitatively: A significant interaction of magnetic particles was reported to start at a filler fraction of $x = 0.2$ independently by Weidenfeller,[63] and Mattei and Le Floc'h.[25] For filler fractions exceeding $x = 0.2$, the mutual influence of particles
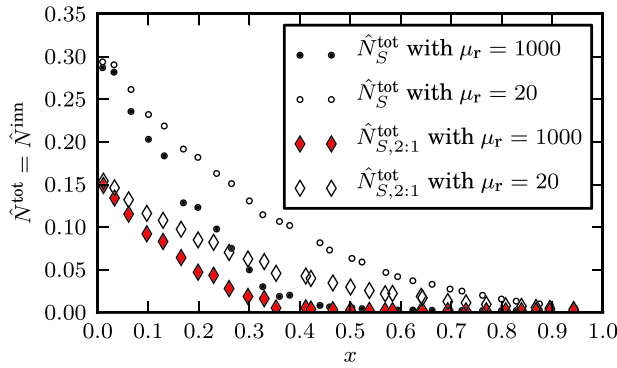
FIG. 8. Comparison of inner DMFs of randomly packed spheres ($\hat{N}_S^{\text{tot}}$) and oriented prolate spheroids ($\hat{N}_{S,2:1}^{\text{tot}}$) with a major to minor aspect ratio of 2 : 1. The DMFs are computed for two different values of magnetic permeability μ_r and various filler fractions x. Results are obtained from simulations of type CI configurations.

FIG. 9. Inner DMF $\hat{N}^{\text{inn}}$ of Fe sample series for eight filler fractions and three orthogonal orientations indicated by subindices 1, 2, and 3 obtained from type CI configurations based on tomography data. Magnetic permeability of particles is set to $\mu_r = 1000$. For comparison the experimentally determined corresponding inner DMFs $N_{\text{exp.}}^{\text{inn}}$ are shown.[50] The fit function $x \mapsto \exp(-3x)/3$ to the experimental data (dashed line) was determined by Anhalt *et al.*[50]

increases with increasing permeability of the magnetic material. Furthermore, for non-ellipsoidal single particles the DMF itself depends on the magnetic permeability and is no longer a factor of shape alone. For instance, the DMF of cylinders with an axis aligned in the field direction decreases with increasing permeability in the whole range of axis to diameter ratios γ, and is more pronounced for large γ.[34]

In geometries created by distributions of hard or penetrable spheres or spheroids rigorous upper and lower bounds were reported to be a valuable tool to determine the effective permittivity[30] or the effective conductivity[55,60] of the heterostructure. Although, due to the aforementionend mathematical analogy, these bounds should also be applicable to the magnetic permeability no such bounds are known for the DMF.

B. Fe sample series

The DMF of Fe samples is simulated in type CI configurations following a TBNS process. Since, as already mentioned above, in this configuration $\hat{N}^{\text{geo}} = 0$ the DMF depends on the SMC's microstructure only and $\hat{N}^{\text{tot}} = \hat{N}^{\text{inn}}$. In order to emphasize that equivalence the latter term $\hat{N}^{\text{inn}}$ will be used hereafter. Samples with nominal filler fraction $x \in \{0.1, 0.2, \ldots, 0.8\}$ are inscribed into the configuration in three different orientations such that one of the three axes $\mathbf{e}_1, \mathbf{e}_2, \mathbf{e}_3$ of the sample's local coordinate system is aligned to the z-axis (cf. Fig. 3). Subscript $d \in \{1, 2, 3\}$ in $\hat{N}_d^{\text{inn}}$ denotes one of these orientations. The results of simulations using the relative magnetic permeability $\mu_r = 1000$ of the bulk are shown in Fig. 9. Since the orientation used in the simulations cannot be related to the orientation used in the experiments the DMFs are sorted such that the largest DMF corresponds to direction $\mathbf{e}_1$, while the smallest DMF relates to direction $\mathbf{e}_3$. This ordering will be used throughout this paper. Note that the actual filler fractions of the SMC cutouts differ from the nominal ones because of the inhomogeneity of the magnetic loading in the samples used. For every mesh, the minimal edge length d_{min} corresponds to 5 μm in physical space and the SMC subset simulated has dimensions $\emptyset$ 0.7 mm $\times$ 1.4 mm. With a mean particle diameter $d_{\text{Fe}} = 88$ μm of the iron-powder the relative numerical error is estimated to be less than 5% (cf. Fig. 5).
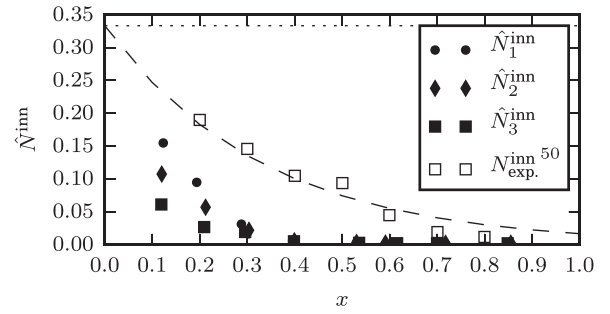
Two issues stand out: (1) The inner DMFs obtained from the simulations strongly deviate from experimental results and (2) the DMFs show a strong anisotropy at $x \in \{0.1, 0.2\}$. The directional 2-point probability functions equally exhibit the observed anisotropy (cf. Fig. 10).

For constant filler fractions larger gradients of $\hat{S}_2$ at $r = 0$ correspond to smaller DMFs. This is also illustrated in Fig. 11 which relates the inner DMFs to the directional specific surface area $\hat{s}_{\mathbf{v}}$ corresponding to the slope of $\hat{S}_2$ at the origin. The data points for different orientations and constant filler fractions $x = 0.1$ and $x = 0.2$ lie approximately on straight lines, whose slopes decrease with increasing filler fractions. For larger filler fractions, this relation cannot be observed and is probably concealed by long range percolation. No simple relation between $\hat{N}^{\text{inn}}$ and $\hat{s}_{\mathbf{v}}$ for varying filler fractions can be found, which is expected since the 2-point probability function contains no information about percolating clusters.

Utilizing the previously generated meshes the Fe samples are further studied with particle permeabilities $\mu_r \in \{10, 20, 50, 100\}$. To account for anisotropy mean values $\langle \hat{N}^{\text{inn}} \rangle = (\hat{N}_1^{\text{inn}} + \hat{N}_2^{\text{inn}} + \hat{N}_3^{\text{inn}})/3$ of the inner DMFs are computed. Figure 12 shows that the experimentally determined DMFs are approached for lower permeabilities. The dependence of the DMF from particle's permeability,
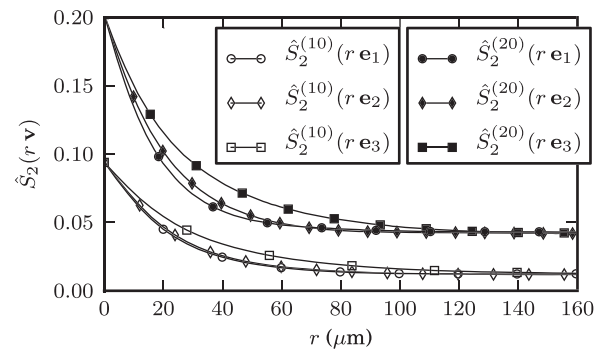

FIG. 10. Directional 2-point probability functions $\hat{S}_2^{(10)}$ and $\hat{S}_2^{(20)}$ for Fe samples and filler fractions $x = 0.1$ and $x = 0.2$, respectively. They are computed along three orthogonal sample orientations $\mathbf{e}_j$ in steps of 1 μm. The superscripts (10) and (20) relate to the considered filler fractions in percent.

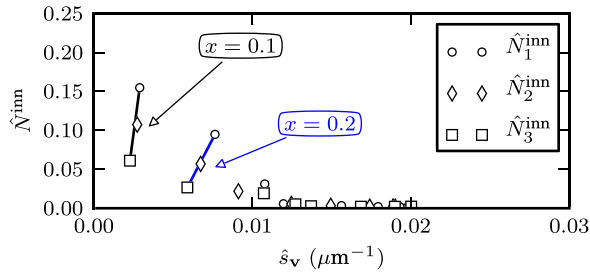FIG. 11. Inner DMFs $\hat{N}_j^{\mathrm{inn}}$ of Fe samples related to the directional specific surface area $\hat{s}_{\mathbf{v}}$ along three orthogonal sample orientations $\mathbf{e}_j$. The DMFs are obtained from type CI configurations with a particle permeability of $\mu_{\mathrm{r}} = 1000$.

already described in Subsection IV A (Fig. 8), can once again clearly be seen in Fig. 12. This behavior was previously described by Mattei.[25] Note that the standard deviation of the DMFs (error bars in Fig. 12) increases with decreasing particle permeability μ_{r} which indicates that the microstructural influence also depends on the particle permeability.

Additionally, apparent permeabilities $\mu_{\mathrm{app},j}$ are determined from this simulation series for each filler fraction and sample orientation $\mathbf{e}_j$. In Fig. 13, the mean value $\langle \mu_{\mathrm{app}} \rangle = (\mu_{\mathrm{app},1} + \mu_{\mathrm{app},2} + \mu_{\mathrm{app},3})/3$ of the apparent permeability is compared to the experimentally measured permeability. The exciting magnetic field strength used is $|\mathbf{H}_0| = 10\,000\,\mathrm{A/m}$.

In the work of Anhalt and Weidenfeller,[11] the experimentally measured permeabilities were compared with mathematical models by Rayleigh, Bruggeman, McLachlan, and others. Only Bruggeman's model described the measured values in the range of $0 \le x \le 0.6$ without making use of fit parameters. Magnetic permeabilities for $x > 0.6$ could only be described by models which were fitted to the experimental data.

For filler fractions $x \le 0.5$, the simulated apparent permeabilities assuming a particle permeability $\mu_{\mathrm{r}} = 50$ are in good agreement with experimental results while they are significantly lower for $x > 0.5$. For a filler fraction of $x = 0.6$, the experimental results coincide with a simulated particle permeability of $\mu_{\mathrm{r}} \approx 100$, and for a filler fraction of $x = 0.8$ experimental and simulated data are in agreement, when a permeability of $\mu_{\mathrm{r}} = 1000$ is assumed.
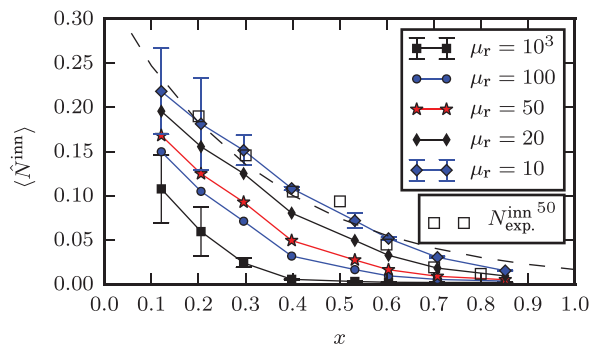

FIG. 12. Mean inner DMFs $\langle \hat{N}^{\mathrm{inn}} \rangle$ of the DMFs of the Fe sample series for three orthogonal directions computed for particle permeabilities $\mu_{\mathrm{r}} \in \{10, 20, 50, 100, 1000\}$. Error bars represent the standard deviation of the DMFs of different orientations. The experimentally determined DMFs $N_{\mathrm{exp.}}^{\mathrm{inn}}$ are shown for reference and taken from Ref. 50. The fit function $x \mapsto \exp(-3x)/3$ to the experimental data (dashed line) is taken from Anhalt *et al.*[50]
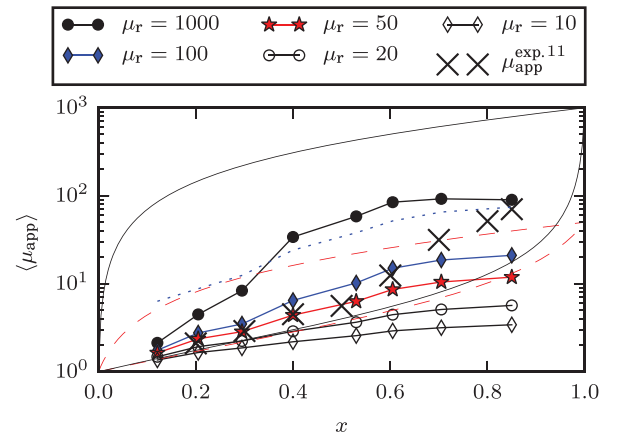

FIG. 13. Mean apparent permeability $\langle \mu_{\mathrm{app}} \rangle$ of Fe sample series computed with particle permeabilities $\mu_{\mathrm{r}} \in \{10, 20, 50, 100, 1000\}$ for eight filler fractions. The experimentally determined apparent permeabilities $\mu\,\mathrm{exp}\cdot_{\mathrm{app}}$ of the samples are shown for reference purposes and taken from the work of Anhalt.[11] The Hashin and Shtrikman lower and upper bounds are plotted for particle permeability $\mu_{\mathrm{r}} = 1000$ (thin solid line) and $\mu_{\mathrm{r}} = 50$ (thin dashed line) using a polymer permeability of $\mu_{\mathrm{poly}} = 1$. The mean of the intrinsic permeability defined in Eq. (7) is plotted for a particle permeability $\mu_{\mathrm{r}} = 100$ (dotted line) and extracted from the mean DMF $\langle \hat{N}^{\mathrm{inn}} \rangle$ using Eq. (9). It naturally provides an upper bound for the corresponding apparent permeability.

Such an extraordinary increase in the permeability was already described by Mattei[64] for filler fractions exceeding $x = 0.6$. Mattei explained this behavior by the agglomeration of particles to several clusters like grains in a bulk material with grain boundaries between these clusters. The generation of such grain like structures leads to cooperative phenomena in domain wall distribution and movement. Because the model used does not include such phenomena a deviation between calculated and experimental values appears. Mattei's hypothesis may be tested by introducing a particle permeability which depends on the particle size or its neighborhood. Once the magnetic permeability is determined as a function of location the numerical simulation is carried out with the same solver as used in this work. A good model for the particle permeability as a function of particle size is crucial for this procedure. Note that the results from simulations using a particle permeability of $\mu_{\mathrm{r}} = 1000$ are farthest away from the experimental results for both, the DMFs and the effective permeabilities, while they are in rather good agreement for smaller particle permeabilities. This corresponds to an experimental study with FeSi composites by Anhalt *et al.*[50] in which a particle permeability of $\mu_{\mathrm{r}} \approx 4$ was measured although the corresponding bulk permeability is $\mu_{\mathrm{r}} \approx 500$.

As mentioned before it is assumed that rigorous lower and upper bounds constructed of functionals of n-point probability functions $S_2(\mathbf{r}^n)$ describe the magnetic permeability below and above the percolation threshold.[55,60] The evaluation of these bounds for 3D real geometries is extremely costly since the computation of the functionals involves integrals of $S_n(\mathbf{r}^n)$ over the entire domain. Instead, the well known but less accurate lower and upper bounds according to the self-consistent model of Hashin and Shtrikman[65] are plotted for an assumed particle permeability of $\mu_{\mathrm{r}} = 1000$ and $\mu_{\mathrm{r}} = 50$ in Fig. 13. In the case of $\mu_{\mathrm{r}} = 1000$, both the

experimental and the simulated data are bounded; whereas for decreasing μ_r the lower bound is trespassed more and more while the upper bound stays in good order. For $\mu_r = 10$ almost all simulated datapoints are below the lower bound of Hashin and Shtrikman (not illustrated). Note that in the configurations considered a natural upper bound to the apparent permeability is given by the intrinsic permeability defined in Eq. (7). Once the DMF is known the intrinsic permeability is determined by Eq. (9).

C. Finemet sample series

Analogously to Subsection IV B, the inner DMFs $\hat{N}^{\mathrm{inn}}$ of the Finemet sample series consisting of four samples with nominal filler fractions $x \in \{0.1, 0.3, 0.4, 0.5\}$ are computed for three orthogonal sample orientations following a TBNS process. Since the mean diameter $d_{\mathrm{Finemet}} = 35\,\mu m$ of the Finemet-powder used is less than half the diameter of the iron powder $d_{\min}$ is set to correspond to $2.5\,\mu m$ to keep the estimated numerical error less than 5%. The SMC subset used has a diameter of 0.35 mm and a length of 0.7 mm.

Simulations using the bulk permeability $\mu_r = 10^5$ of Finemet lead to linear systems which were not solvable with the iterative solvers available. This might be caused by the extreme jump of the relative permeability at magnetic-nonmagnetic interfaces. In first approximation, the particle permeability is reduced to smaller values. The results of the
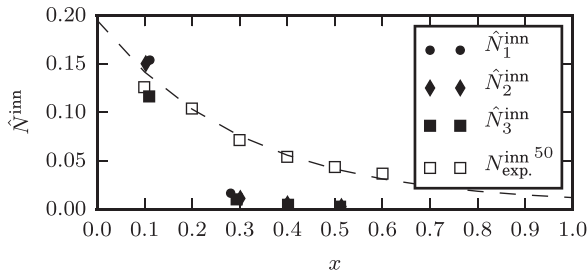
FIG. 14. Inner DMFs $\hat{N}^{\mathrm{inn}}$ of Finemet sample series for four filler fractions and three orthogonal sample orientations indicated by subindices 1, 2, and 3 obtained from type CII configurations based on tomography data. Particle permeability is set to $\mu_r = 1000$. The experimentally determined corresponding DMFs[50] $N^{\mathrm{inn}}_{\mathrm{exp.}}$ are depicted for reference. The fit function $x \mapsto 0.19\exp(-3.3\,x) + 0.005$ to the experimental data (dashed line) was determined by Anhalt *et al.*[50]
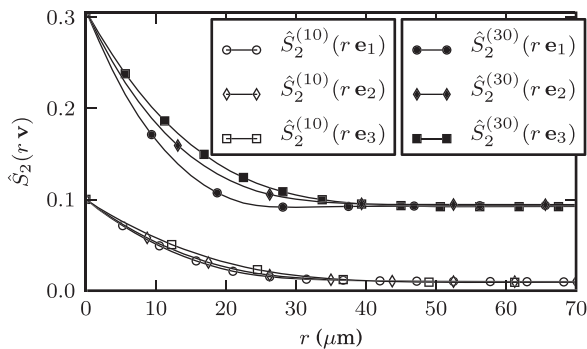
FIG. 15. Directional 2-point probability functions $\hat{S}_2^{(10)}$ and $\hat{S}_2^{(30)}$ for Finemet samples and filler fractions $x = 0.1$ and $x = 0.3$, respectively. They are computed along three orthogonal sample orientations $\mathbf{e}_j$ in steps of $1\,\mu m$. The superscripts (10) and (30) relate to the considered filler fractions in percent.
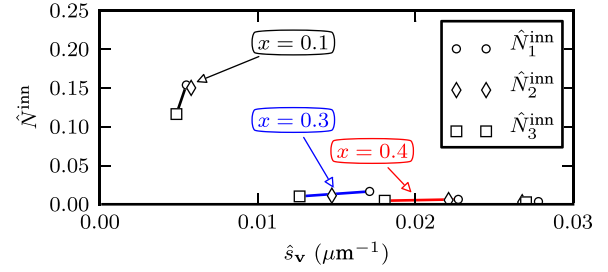
FIG. 16. Inner DMFs $\hat{N}^{\mathrm{inn}}_j$ of Finemet samples related to the directional specific surface area $\hat{s}_{\mathbf{v}}$ along three orthogonal sample orientations $\mathbf{e}_j$. The DMFs are obtained from type CII configurations with an assumed particle permeability of $\mu_r = 1000$.

simulation study computed with particle permeability $\mu_r = 1000$ are shown in Fig. 14. The observations regarding the inner DMFs are analogous to that in Subsection IV B.

As before directional 2-point probability functions are computed for the Finemet samples. They are depicted in Fig. 15. The observations from Subsection IV B recur: the DMFs obtained from simulations for constant filler fractions are largest for steepest and smallest for flattest $\hat{S}_2$ curves at $r = 0$. Again, no simple relation of DMFs and $\hat{s}_{\mathbf{v}}$ for different filler fractions can be found, see Fig. 16. The previously generated meshes are additionally used for a set of simulations with smaller particle permeabilities $\mu_r \in \{10, 20, 50, 100\}$. The mean value $\langle \hat{N}^{\mathrm{inn}} \rangle$ of the three DMFs of orthogonal directions are computed for each filler fraction, see Fig. 17. Good agreement between experiment and simulation is observed for a relative permeability $\mu_r = 50$, which is significantly smaller than the bulk permeability $\mu_r = 10^5$ of Finemet.

It is remarkable, that—despite of the differences in permeability values of Fe and Finemet—the experimental and calculated results for filler fractions $x \leq 0.5$ are in good agreement for an assumed particle permeability of $\mu_r = 50$. Nevertheless, this finding corresponds to previous permeability measurements of various SMCs, which all show nearly the same permeability for filler fractions $x \leq 0.5$ despite of the magnetic material used.[63]
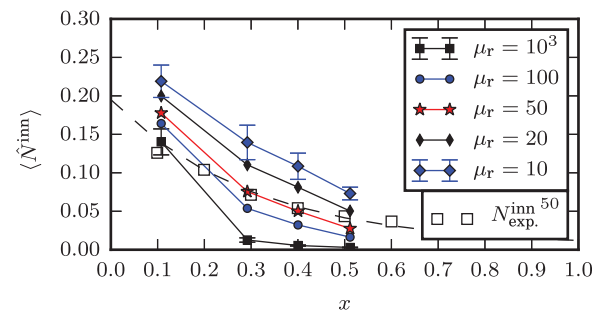
FIG. 17. Mean inner DMFs $\langle \hat{N}^{\mathrm{inn}} \rangle$ of the DMFs of Finemet sample series for three orthogonal directions. They are computed for four filler fractions and for particle permeabilities $\mu_r \in \{10, 20, 50, 100, 1000\}$. Error bars represent the standard deviation of the DMFs of different orientations. Experimentally determined DMFs $N^{\mathrm{inn}}_{\mathrm{exp.}}$ (Ref. 50) of the identical samples are shown for reference. The fit function $x \mapsto 0.19\exp(-3.3\,x) + 0.005$ to the experimental data (dashed line) was determined by Anhalt *et al.*[50]

V. DISCUSSION

In this work, the influence of the microstructure of soft magnetic composites (SMCs) on the demagnetizing factor (DMF) was studied using tomography based numerical simulation (TBNS). TBNS provides very detailed magnetic field information. Simulations show that microgeometry strongly affects the DMFs. This can be observed in the significant variance of the DMFs for small filler fractions. The variance is larger for small particle permeabilities μ_r and smaller for large particle permeabilities. It vanishes above a percolation limit which itself depends on the particle permeability. For $\mu_r = 1000$, the percolation limit occurs at a filler fraction $x_P \approx 0.35$. The percolation limit for $\mu_r < 1000$ can be found at larger filler fractions. Above the percolation limit, the microgeometry of the SMC no longer affects the DMF of the SMC. Generally agglomeration and clustering seem to govern the DMF of SMCs in the complete range $x \in [0, 1]$. With increasing filler fraction particles come close enough to interact. Following the pole avoidance principle they combine to larger magnetic particles resulting in a lower DMF. At the same time, the formation of such clusters reduces the influence of the microgeometry. Eventually, the percolation threshold is reached, above which the SMCs' DMF is governed by its macroscopic shape alone and approaches the linear law $\hat{N}^{tot}(x) = N^{geo} \times x$.

The DMF and the derivative of a 2-point probability function at its origin are linearly related for different orientations and for fixed small filler fractions. However, there does not seem to be any simple relation accounting for different filler fractions.

Based on the results of this TBNS study and their experimental counterparts,[50] we conjecture that the particle permeability of SMCs is orders of magnitude smaller than their bulk permeability which is in accordance with a former study of Le Floc'h *et al.*[22] who attributed this to a reduced domain wall mobility due to a strong adherence of domain walls to particle edges. The low number of moveable domain walls in SMCs was later shown by Anhalt.[4]

However, uncertainties regarding the comparison between TBNS and the experiment arise both from (1) the experimental and (2) the TBNS side. On the experimental side, it is difficult to isolate single quantities such as the DMF from indirect measurements. On the TBNS side, the reliability of results is limited by the underlying model assumptions (e.g., linear material response). In addition, the geometric resolution of μCT scans is limited and computer memory restricts the size of the domain that can be simulated.

The relative errors in the numerical procedure used are estimated to be less than 5%. DMFs obtained from computer generated artificial SMCs are in good agreement with the work of Mattei and Le Floc'h[25] who used random sphere packings on a grid.

This work demonstrates that TBNS is applicable to magnetostatic phenomena and provides a tool to investigate magnetic properties. The simulation results obtained in this study confirm the massive influence of microstructure, agglomeration, and percolation on the magnetic properties of SMCs and heterogeneous magnetic materials. The 4.5 TB of electromagnetic field data produced provides a rich source for further research and can be obtained from the authors at any time.

[1]L. Svensson, K. Frogner, P. Jeppsson, T. Cedell, and M. Andersson, J. Magn. Magn. Mater. **324**, 2717 (2012).
[2]L. O. Hultman and A. G. Jack, in *Electric Machines and Drives IEEE International Conference* (IEEE, 2003), Vol. 1, pp. 516–522.
[3]H. Shokrollahi and K. Janghorban, J. Mater. Process. Technol. **189**, 1 (2007).
[4]M. Anhalt and B. Weidenfeller, J. Magn. Magn. Mater. **304**, e549 (2006).
[5]A. Taghvaei, H. Shokrollahi, K. Janghorban, and H. Abiri, Mater. Des. **30**, 3989 (2009).
[6]E. Salahun, G. Tanne, P. Queffelec, P. Gelin, A.-L. Adenot, and O. Acher, in *Microwave, MTT-S International Symposium* (IEEE, 2002), Vol. 2, pp. 1185–1188.
[7]J. Zhu and Y. Guo, in *Conference Record of the 2004 IEEE Industry Applications Conference, 39th IAS Annual Meeting* (IEEE, 2004), pp. 373–380.
[8]A. Reinap, M. Alaküla, T. Cedell, M. Andersson, and P. Jeppsson, in *Proceedings of the 2008 International Conference on Electrical Machines*, ICEM 2008, 18th International Conference on Electrical Machines (IEEE, 2009), pp. 2293–2297.
[9]A. Reinap, M. Alaküla, G. Lindstedt, B. Thuresson, T. Cedell, M. Andersson, and P. Jeppsson, in *Proceedings of the 2008 International Conference on Electrical Machines*, ICEM 2008, 18th International Conference on Electrical Machines (IEEE, 2009), pp. 2288–2292.
[10]Y. Guo, J. Zhu, D. Dorrell, H. Lu, and Y. Wang, in *IEEE Energy Conversion Congress and Exposition* (IEEE, 2009), pp. 294–301.
[11]M. Anhalt and B. Weidenfeller, J. Appl. Phys. **101**, 023907 (2007).
[12]M. Anhalt, J. Magn. Magn. Mater. **320**, e366 (2008).
[13]M. Anhalt and B. Weidenfeller, Mater. Sci. Eng., B **162**, 64 (2009).
[14]P. Kollár, Z. Birčáková, J. Füzer, R. Bureš, and M. Fáberová, J. Magn. Magn. Mater. **327**, 146 (2013).
[15]K. Rozanov, A. Osipov, D. Petrov, S. Starostenko, and E. Yelsukov, J. Magn. Magn. Mater. **321**, 738 (2009).
[16]J.-L. Mattei and M. Le Floc'h, J. Magn. Magn. Mater. **264**, 86 (2003).
[17]I. Hemmati, H. M. Hosseini, and A. Kianvash, J. Magn. Magn. Mater. **305**, 147 (2006).
[18]A. Taghvaei, H. Shokrollahi, M. Ghaffari, and K. Janghorban, J. Phys. Chem. Solids **71**, 7 (2010).
[19]C. Brosseau and P. Talbot, Meas. Sci. Technol. **16**, 1823 (2005).
[20]C. Brosseau, W. NDong, and A. Mdarhri, J. Appl. Phys. **104**, 074907 (2008).
[21]E. Kneller, *Ferromagnetismus* (Springer, Berlin Heidelberg, 1962).
[22]M. Le Floc'h, J. Mattei, P. Laurent, O. Minot, and A. Konn, J. Magn. Magn. Mater. **140–144**, 2191 (1995).
[23]J. Mattei, P. Laurent, O. Minot, and M. Le Floc'h, J. Magn. Magn. Mater. **160**, 23 (1996).
[24]A. Chevalier and M. Le Floc'h, J. Appl. Phys. **90**, 3462 (2001).
[25]J.-L. Mattei and M. Le Floc'h, J. Magn. Magn. Mater. **257**, 335 (2003).
[26]V. B. Bregar and M. Pavlin, J. Appl. Phys. **95**, 6289 (2004).
[27]V. Bregar, Phys. Rev. B **71**, 174418 (2005).
[28]S. Torquato, *Random Heterogeneous Materials: Microstructure and Macroscopic Properties*, Interdisciplinary Applied Mathematics (Springer, Berlin, 2002).
[29]V. Myroshnychenko and C. Brosseau, Phys. Rev. E **71**, 016701 (2005).
[30]V. Myroshnychenko and C. Brosseau, J. Appl. Phys. **97**, 044101 (2005).
[31]A. Mejdoubi and C. Brosseau, J. Appl. Phys. **99**, 063502 (2006).
[32]V. Myroshnychenko and C. Brosseau, J. Appl. Phys. **103**, 084112 (2008).
[33]M. Sato and Y. Ishii, J. Appl. Phys. **66**, 983 (1989).
[34]D.-X. Chen, J. A. Brug, and R. B. Goldfarb, IEEE Trans. Magn. **27**, 3601 (1991).
[35]D.-X. Chen, E. Pardo, and A. Sanchez, IEEE Trans. Magn. **38**, 1742 (2002).

[36]D. Chen, E. Pardo, and A. Sanchez, IEEE Trans. Magn. **41**, 2077 (2005).

[37]M. Beleggia, D. Vokoun, and M. D. Graef, J. Magn. Magn. Mater. **321**, 1306 (2009).

[38]N. S. Walmsley, R. W. Chantrell, J. G. Gore, and M. Maylin, J. Phys. D: Appl. Phys. **33**, 784 (2000).

[39]B. Drnovšek, V. B. Bregar, and M. Pavlin, J. Appl. Phys. **105**, 07D546 (2009).

[40]J.-L. Mattei and M. Le Floc'h, J. Magn. Magn. Mater. **215–216**, 589 (2000).

[41]B. Drnovšek, V. B. Bregar, and M. Pavlin, J. Appl. Phys. **103**, 07D924 (2008).

[42]E. N. Landis and D. T. Keane, Mater. Charact. **61**, 1305 (2010).

[43]GE Measurement & Control: Phoenix nanotom m, 2014, available at http://www.ge-mcs.com/en/radiography-x-ray/ct-computed-tomography/phoenix-nanotom-m.html (last accessed: September 18, 2014).

[44]H. Friess, S. Haussener, A. Steinfeld, and J. Petrasch, Int. J. Numer. Methods Eng. **93**, 1040 (2013).

[45]A. Bossavit, IEE Proc. A **135**, 493 (1988).

[46]Elmer (rev.: 6509m), 2014, available at http://www.csc.fi/elmer (last accessed September 18, 2014).

[47]A. Akolkar and J. Petrasch, Int. J. Heat Mass Transfer **54**, 4775 (2011).

[48]J. Petrasch, B. Schrader, P. Wyss, and A. Steinfeld, J. Heat Transfer **130**, 032602 (2008).

[49]J. Petrasch, F. Meier, H. Friess, and A. Steinfeld, Int. J. Heat Fluid Flow **29**, 315 (2008).

[50]M. Anhalt, B. Weidenfeller, and J. Mattei, J. Magn. Magn. Mater. **320**, e844 (2008).

[51]J. Paterson, S. Cooke, and A. Phelps, J. Magn. Magn. Mater. **177–181**, 1472 (1998).

[52]E. Dussler, Z. Phys. **44**, 286 (1927).

[53]S. Stock, *MicroComputed Tomography: Methodology and Applications* (CRC Press, 2008).

[54]S. Rajagopalan, L. Lu, M. Yaszemski, and R. Robb, J. Biomed. Mater. Res. Part A **75A**, 877 (2005).

[55]I. Kim and S. Torquato, J. Appl. Phys. **71**, 2727 (1992).

[56]M. Tancrez and J. Taine, Int. J. Heat Mass Transfer **47**, 373 (2004).

[57]R. Landauer, in *Electrical Transport and Optical Properties of Inhomogeneous Media*, edited by J. Garland and D. Tanner (AIP, New York, 1978), pp. 32–42.

[58]S. Torquato and Y. Jiao, J. Chem. Phys. **137**, 074106 (2012).

[59]S. Torquato, J. Chem. Phys. **136**, 054106 (2012).

[60]S. Torquato and F. Lado, J. Chem. Phys. **94**, 4453 (1991).

[61]Salome—the open source integration platform for numerical simulations, 2014, available at http://www.salome-platform.org/ (last accessed September 18, 2014).

[62]Visualization toolkit (vtk), 2014, available at http://www.vtk.org/ (last accessed December 17, 2014).

[63]B. Weidenfeller, *Polymer Bonded Soft Magnetic Composites* (Papierflieger, Clausthal-Zellerfeld, 2008).

[64]J. Mattei, A. Konn, and M. Le Floc'h, IEEE Trans. Instrum. Meas. **42**, 121 (1993).

[65]Z. Hashin and S. Shtrikman, J. Appl. Phys. **33**, 3125 (1962).